Supporting Information

Metallasilsesquioxanes Derived Ultrathin Porous Carbon Nanosheets 3D Architectures via "In-situ Dual Templating" Strategy for Ultrafast Sodium Storage

Xieji Lin,[a] Yue Dong,[a] Xiaohong Chen,[a] Haiyan Liu,[b] Zhaobin Liu,[b] Tao Xing,[b] Ang Li*[a] and Huaihe Song*[a]

[a] State Key Laboratory of Chemical Resource Engineering, Beijing Key Laboratory of Electrochemical Process and Technology for Materials, Beijing University of Chemical Technology, Beijing, 100029, P. R. China.

[b] Yankuang Group CO. LTD., Tengzhou, Shandong 277527, P.R. China.

E-mail: thorne22003@163.com, songhh@mail.buct.edu.cn.

We denote the pyrolytic products at different carbonization temperatures S-x, and porous carbon nanosheets architectures obtained at different carbonization temperatures PCNS-x, where x is the carbonization temperature in the Supplementary Information for convenience.

Supplementary Figures

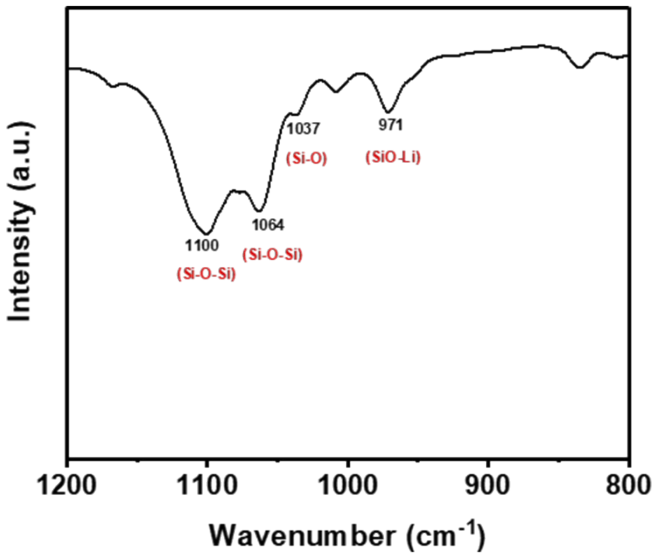

Fig.S1 FT-IR spectrum of Lithium hepta(i-butyl) silsesquioxane trisilanolate (T7-Li).

As shown in Fig.S1, the symmetric *v*Si-OLi stretches can be observed at 971 cm^{-1}, which is characteristic bond for box-shaped Li_6O_6 in T7-Li. And the silsesquioxane framework was characterized by *v*Si-O-Si stretches at 1064 and 1100 cm^{-1}. These results are well consistent with the previous report,[S1] indicating the well-defined structure of T7-Li.

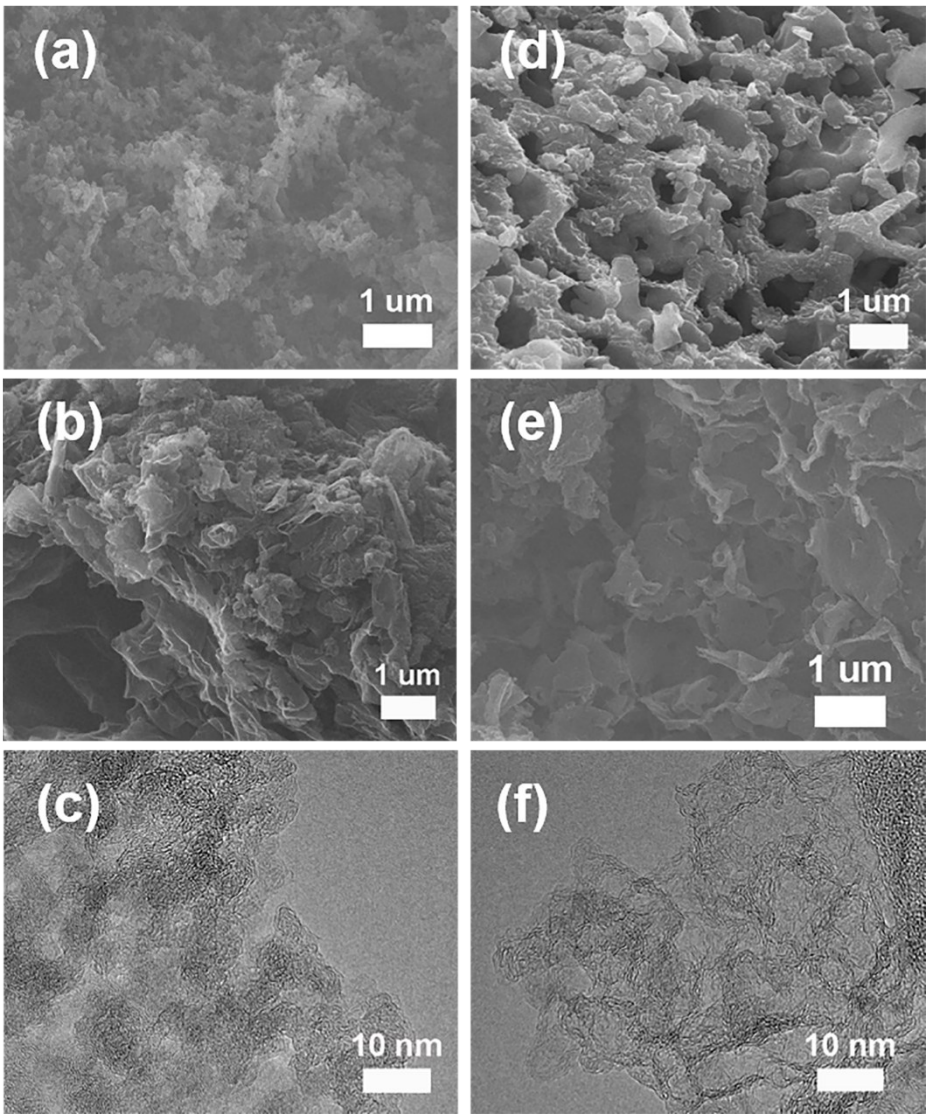

Fig.S2 (a) SEM image of S-700, (b, c) SEM image and HRTEM image of PCNS-700.

(d) SEM image of S-800, and (e, f) SEM image and HRTEM image of PCNS-800.

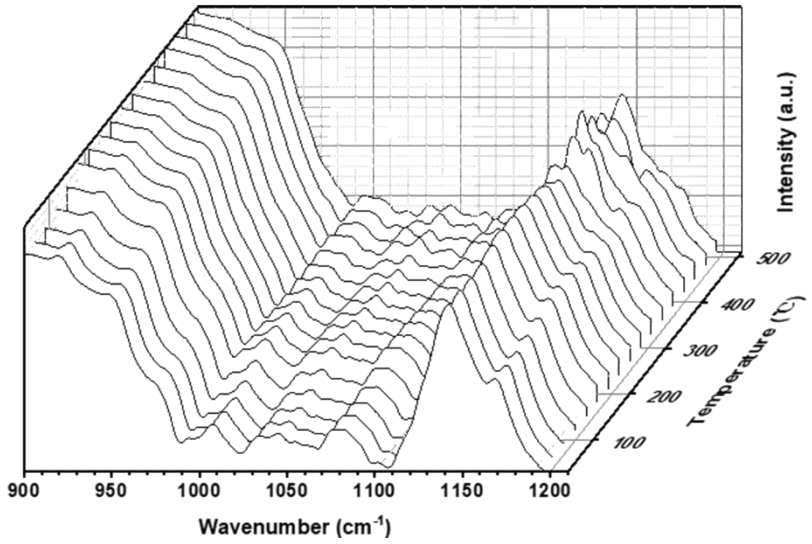

Fig.S3 In-situ FT-IR spectra of T7-Li from 30 to 510℃.

To further investigate the formation process of lithium silicate, the in-situ FT-IR spectra were carried out to collect the change of Si-O-Si in T7-Li, the results were shown in Fig.S3. It can be observed obviously that the characteristics peak of Si-O-Si in T7-Li at ~1130 cm^{-1} disappears when the temperature reaches 360 ℃, suggesting the pyrolysis of inorganic core in T7-Li. Meanwhile, the two shoulder peaks at 1100-1150 cm^{-1} appear, corresponding to the Si-O in silicon oxide[S2], which indicates that the formation of SiO_2 during the initial state of calcination. Interestingly, the peaks become stronger and the blue-shift also occurs with the increasing temperature. This phenomenon would be attributed to the formation of lithium silicate caused by reaction between silica nanoparticles and lithium oxide.[S3-5]

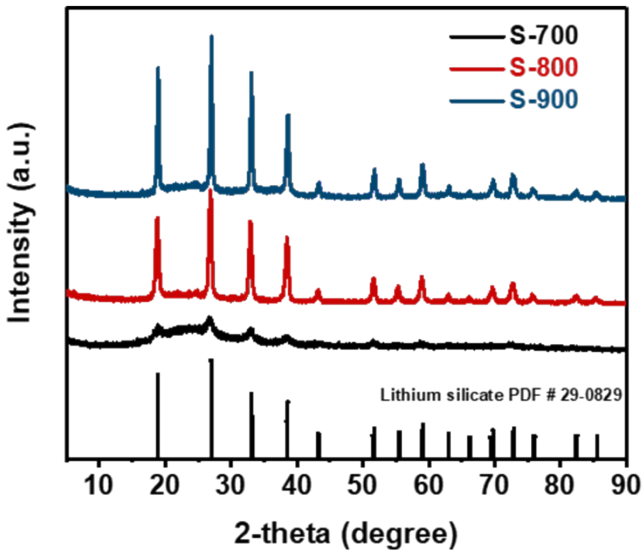

Fig.S4 XRD patterns of S-700, S-800, and S-900, respectively.

Fig.S4 exhibits the XRD patterns of the pyrolytic products at different carbonization temperatures without etching, respectively. The peaks at 18.9, 27.0, 33.1, and 38.7 ° can be found among the three samples, which corresponds to the Lithium silicate (PDF #29-0828). The intensity of the peak increases with the higher calcination temperature indicating the better degree of crystallization of lithium silicate.

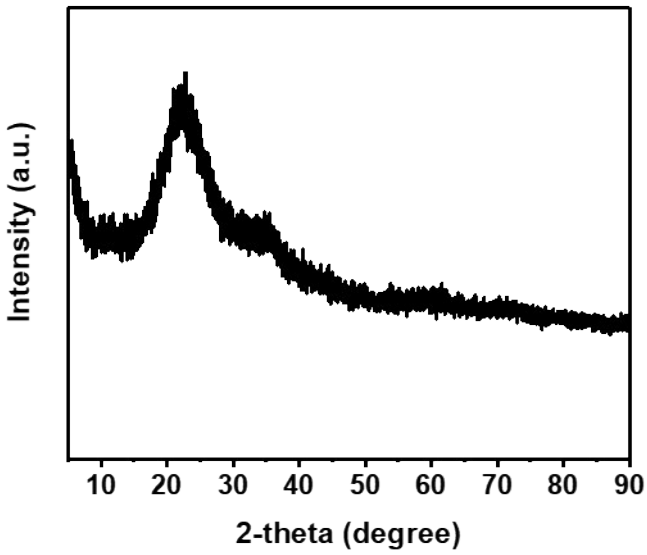

Fig.S5 XRD pattern of the product obtained by removing lithium silicate of S-900.

XRD pattern of product obtained by removing lithium silicate of S-900 was obtained to verify the completely removal of lithium silicate, which is shown in Fig.S5. A broad and dispersive diffraction peak at about 25 ^{o} can be detected and no peaks corresponding to lithium silicate can be observed, which can be ascribed to the completely removal of lithium silicate.

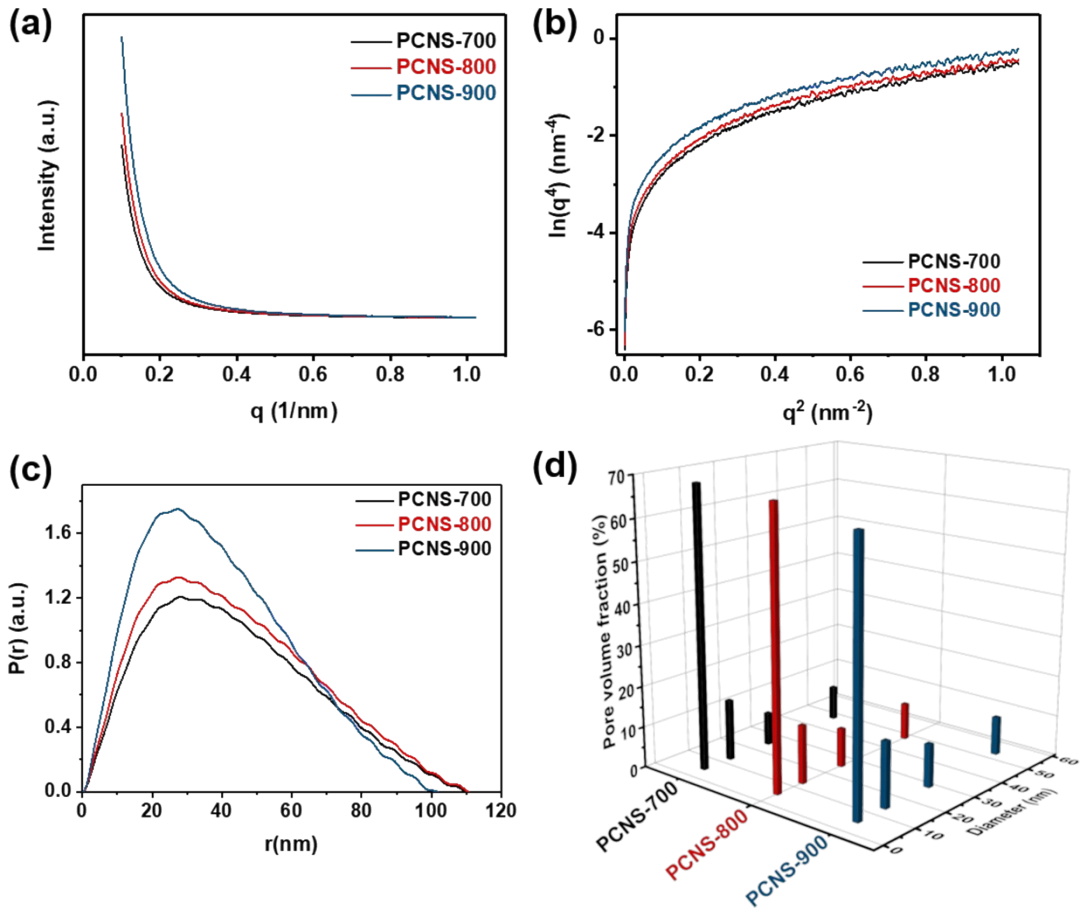

Fig.S6 (a) SAXS curves of PCNSs, (b) porod plot with point-collimation in SAXS, (c) distance distribution function, (d) the pore size distribution of PCNSs obtained by SAXS.

The SAXS was carried out to further investigate the porous property characterization of PCNSs, and the results are displayed in Fig.S6. And the porous property characterization of PCNSs can be obtained by Porod's law as the following equation:[S6,S7]

$$I(q) = \frac{K}{q^4} exp(bq^2) \qquad (S1)$$

Where I(q) is the scattering intensity, q is the scattering vector, $q=4\pi\sin\theta/\lambda$, 2θ is the scattering angle, K is the Porod constant, and b is a constant related to the size of regions with micro-fluctuations of electron density.

$$S_V = \pi P(1-P)\frac{K}{Q} \qquad (S2)$$

Where S_v is the total surface per unit of volume, P is the porosity of the sample, and Q is the invariant constant, which is obtained by:

$$Q = \int_0^\infty qI(q)dq \qquad (S3)$$

And SAXS method can also be applied to simulate the scatterer size distribution, which can be described as:[S6,S7]

$$I(q) = C\int_0^\infty D_V(r)r^3 I_0(q,r)dr \qquad (S4)$$

Where C is a constant, $D_v(r)$ is defined as the volume distribution of scatterer with size r. $I_0(q,r)$ is the scattering intensity of the radially symmetric scatterer of size r. The determination of $D_V(r)$ is the key to calculate the pore distribution, and we used the cascade tangent rule of Jellinek method based on Guinier's approach:

$$\bar{r} = \sum r_i D_{Vi} \qquad (S5)$$

Furthermore, the fractal characterization of PCNSs can be also obtained by SAXS method. The SAXS intensity of fractal samples have a power-law form:

$$I(q) = I_0 q^{-\alpha} \qquad (S6)$$

Where I_0 and α are constant.

For porous fractal, the porous fractal dimension D_p is given by:

$$D_P = \alpha,\ 1 < \alpha < 3 \qquad (S7)$$

Whereas for surface fractal, the surface fractal dimension D_S is given by:

$$D_S = 6 - \alpha, 3 < \alpha < 4 \qquad (S8)$$

And the results calculated by SAXS are presented in Table S3 and S4.

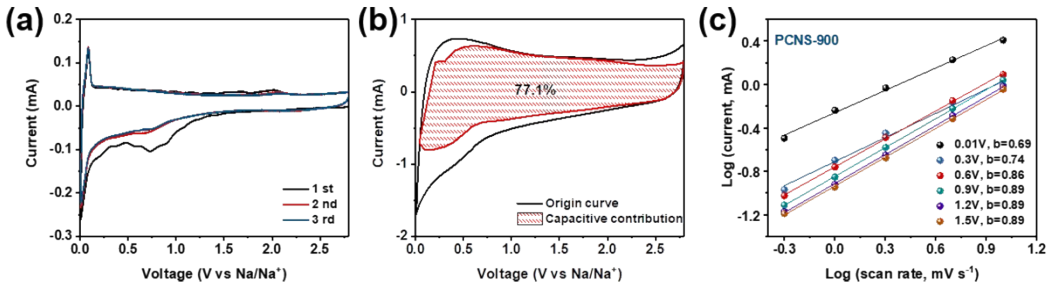

Fig.S7 (a) CV curves at a scan rate of 0.2 mV s^{-1}, (b) CV curves at a scan rate of 5 mV s^{-1} with capacitive currents (k_1v) being plotted at certain potentials, and (c) linear relationships between the logarithm currents log (i) and logarithm scan rates log (v) of PCNS-900.

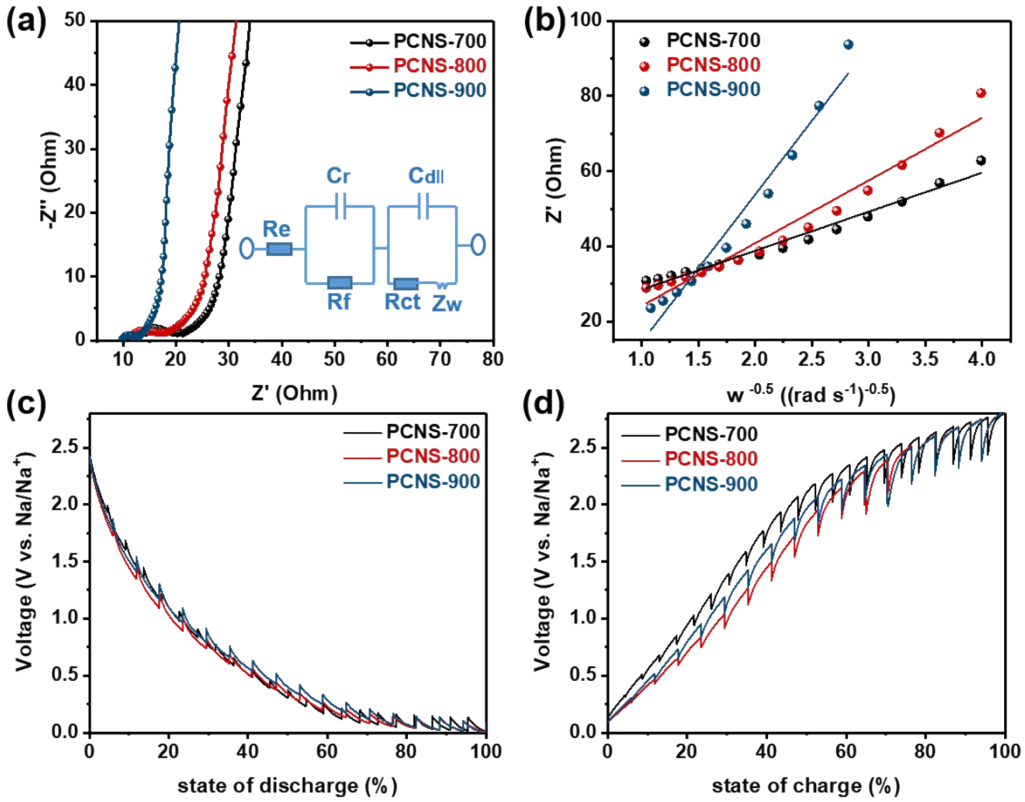

Fig.S8 Electrcohemical impedance of PCNSs, (a) Nyquist plots, (b) resistance fitting results. GITT curves of PCNSs in the potential range of 0.01 – 2.8 V at discharge

/charge current density of 50 uA for each pulse for 15 min and following relaxation for 60 min, (c) discharge and (d) charge process.

Supplementary Tables

Table S1. The results of XPS.

Samples	C at%	O at%
PCNS-700	91.06	8.94
PCNS-800	93.76	6.24
PCNS-900	90.01	9.99

Table S2. BET parameters of PCNSs obtained by N_2 adsorption-desorption isotherms.

Samples	$S^{a)}_{BET}$ ($m^2\ g^{-1}$)	$S^{b)}_{meso}$ ($m^2\ g^{-1}$)	$V^{c)}_{total}$ ($cm^3\ g^{-1}$)	$V^{d)}_{meso}$ ($cm^3\ g^{-1}$)	$D^{e)}_{average}$ (nm)
PCNS-700	1065.3	906.6	2.63	2.49	9.88
PCNS-800	1056.0	963.0	2.79	2.67	10.58
PCNS-900	1022.7	987.8	2.97	2.89	11.61

[a)] Specific surface area calculated by BET method.

[b)] Specific surface area of mesopores calculated by BJH method.

[c)] Total pore volume.

[d)] Volume of mesopores.

[e)] Average diameter of pore obtained by N_2 adsorption-desorption isotherms.

Table S3. The porosity parameters of samples obtained by SAXS.

Samples	$S^{a)}_{SAXS}$ ($m^2\ g^{-1}$)	$D^{b)}_{average}$ (nm)	$t_c^{c)}$ (nm)	$l_c^{d)}$ (nm)	$D^{e)}$ (nm)
PCNS-700	1186.6	11.16	4.67	8.03	11.16
PCNS-800	1257.8	11.91	4.90	8.33	11.91
PCNS-900	1286.9	13.56	5.30	8.70	13.56

a) Specific surface area calculated by SAXS method.

b) Average pore size.

c) Correlation distance.

d) Average carbon wall thickness.

e) Average diameter of pore obtained by SAXS.

Table S4. The fractal parameters of samples obtained by SAXS.

Samples	Pore size (nm)	Fractal dimension
PCNS-700	6.14-15.88	2.02
	21.61-50.08	2.50
	77.94-143.29	1.79
PCNS-800	6.14-19.63	2.05
	23.12-49.89	2.62
	75.01-143.29	1.72
PCNS-900	6.14-19.56	2.14
	23.21-49.97	2.65

	71.43-143.29	1.68

Table S5. Kinetics parameters of PCNSs.

Samples	R_e	R_f	R_{ct}
PCNS-700	14.15	4.02	2.26
PCNS-800	11.77	3.18	2.22
PCNS-900	9.86	0.69	1.56

Table S6. Performance comparison between previous report and our work.

Samples	Reversible capacity	Rate performance	Ref.
PCNS-900	330.5 mA h g^{-1} at 0.1A g^{-1}	230.5 mA h g^{-1} at 10 A g^{-1}	This work
PCNS-800	346.6 mA h g^{-1} at 0.1 A g^{-1}	163.9 mA h g^{-1} at 10 A g^{-1}	This work
PCNS-700	261.3 mA h g^{-1} at 0.1 A g^{-1}	125 mA h g^{-1} at 10 A g^{-1}	This work
3D N,O and P heteroatoms porous carbon	332 mA h g^{-1} at 0.05 A g^{-1}	139 mA h g^{-1} at 10 A g^{-1}	S8
Hierarchical N/S co-doped carbon	248 mA h g^{-1} at 0.05 A g^{-1}	74 mA h g^{-1} at 10 A g^{-1}	S9
P doped 3D	270 mA h g^{-1} at 0.2 A g^{-1}	140 mA h g^{-1} at 10 A g^{-1}	S10

porous carbon			
N-rich carbon nanosheets	317 mA h g^{-1} at 0.1 A g^{-1}	194 mA h g^{-1} at 10 A g^{-1}	S11
3D hollow porous carbon microspheres	313.8 mA h g^{-1} at 0.1 A g^{-1}	112.5 mA h g^{-1} at 5 A g^{-1}	S12
3D porous carbon frameworks	290 mA h g^{-1} at 0.2 A g^{-1}	104 mA h g^{-1} at 10 A g^{-1}	S13
Porous carbon nanosheets	300 mA h g^{-1} at 0.05 A g^{-1}	74 mA h g^{-1} at 5 A g^{-1}	S14
N-doped carbon nanotubes	192 mA h g^{-1} at 0.5 A g^{-1}	103 mA h g^{-1} at 10 A g^{-1}	S15
N,P co-doped carbon networks	223 mA h g^{-1} at 0.05 A g^{-1}	145 mA h g^{-1} at 10 A g^{-1}	S16
N-doped interconnecte	150 mA h g^{-1} at 0.2 A g^{-1}	73 mA h g^{-1} at 20 A g^{-1}	S17

d carbon nanofibers			
Mesoporous soft carbon	331 mA h g^{-1} at 0.03 A g^{-1}	103 mA h g^{-1} at 0.5 A g^{-1}	S18
Nanoporous N-doped carbon	496 mA h g^{-1} at 0.03 A g^{-1}	280 mA h g^{-1} at 5 A g^{-1}	S19
2D heteroatom-doped carbon	308 mA h g^{-1} at 0.2 A g^{-1}	225 mA h g^{-1} at 1 A g^{-1}	S20

Supplementary References

S1. Prigyai, N.; Chanmungkalakul, S.; Ervithayasuporn, V.; Yodsin, N.; Jungsuttiwong, S.; Takeda, N.; Unno, M.; Boonmak, J.; Kiatkamjornwong, S., *Inorg. Chem.* **2019,** *58* (22), 15110-15117.

S2. Zheng, J.; Han, D.; Ye, X.; Wu, X.; Wu, Y.; Wang, Y.; Zhang, L., *Polymer* **2018,** *135*, 200-210.

S3. Marler, B.; Muller, M.; Gies, H., *Dalton. Trans.* **2016,** *45* (25), 10155-64.

S4. Vidal, L.; Joussein, E.; Colas, M.; Cornette, J.; Sanz, J.; Sobrados, I.; Gelet, J. L.; Absi, J.; Rossignol, S., *Colloid. Surfaces A* **2016,** *503*, 101-109.

S5. Supriya, N.; Rajeev, R., *J Therm. Anal. Calorim.* **2020**.

S6. Z. Li, Chinese Phys. C 2013, 37.

S7. A. Li, Y. Tong, B. Cao, H. Song, Z. Li, X. Chen, J. Zhou, G. Chen, H. Luo, Sci. Rep. 2017, 7, 40574.

S8. Zhou, C.; Wang, D.; Li, A.; Pan, E.; Liu, H.; Chen, X.; Jia, M.; Song, H., *Chem. Eng. J.* **2020,** *380*.

S9. Shao, W.; Hu, F.; Song, C.; Wang, J.; Liu, C.; Weng, Z.; Jian, X., *J Mater. Chem. A* **2019,** *7* (11), 6363-6373.

S10. Qiao, Y.; Han, R.; Pang, Y.; Lu, Z.; Zhao, J.; Cheng, X.; Zhang, H.; Yang, Z.; Yang, S.; Liu, Y., *J Mater. Chem. A* **2019,** *7* (18), 11400-11407.

S11. Liu, S.; Zhou, J.; Song, H., *Adv. Energy Mater.* **2018,** *8* (22).

S12. Zou, G.; Hou, H.; Cao, X.; Ge, P.; Zhao, G.; Yin, D.; Ji, X., *J Mater. Chem. A* **2017,** *5* (45), 23550-23558.

S13. Hou, H.; Banks, C. E.; Jing, M.; Zhang, Y.; Ji, X., *Adv. Mater.* **2015,** *27* (47),

7861-6.

S14. Yoon, D.; Kim, D. H.; Chung, K. Y.; Chang, W.; Kim, S. M.; Kim, J., *Carbon* **2016,** *98*, 213-220.

S15. Wei, R.; Huang, M.; Ma, W.; Xi, B.; Feng, Z.; Li, H.; Feng, J.; Xiong, *J Energy Chem.* **2020,** *49*, 136-146.

S16. Wang, H.; Yuan, H.; Zhan, W.; Lee, Y.-S.; Shin, H.-J.; Wei, X.; Cai, Q.; Lan, J.-L.; Yu, Y.; Yang, X., *Carbon* **2020,** *165*, 204-215.

S17. Wang, Z.; Qie, L.; Yuan, L.; Zhang, W.; Hu, X.; Huang, Y., *Carbon* **2013,** *55*, 328-334.

S18. Cao, B.; Liu, H.; Xu, B.; Lei, Y.; Chen, X.; Song, H., *J Mater. Chem. A* **2016,** *4* (17), 6472-6478.

S19. Mehmood, A.; Ali, G.; Koyutürk, B.; Pampel, J.; Chung, K. Y.; Fellinger, T.-P., *Energy Storage Mater.* **2020,** *28*, 101-111.

S20. Jin, Q.; Li, W.; Wang, K.; Li, H.; Feng, P.; Zhang, Z.; Wang, W.; Jiang, K., *Adv. Funct. Mater.* **2020,** *30* (14).